Pressure-induced superconductivity in Li-Te electrides

Xiaohua Zhang [1,2] Fei Li [1] Aitor Bergara,[3,4,5,*] and Guochun Yang[1,2,†]

[1]*State Key Laboratory of Metastable Materials Science & Technology and Key Laboratory for Microstructural Material Physics of Hebei Province, School of Science, Yanshan University, Qinhuangdao 066004, China*

[2]*Centre for Advanced Optoelectronic Functional Materials Research and Key Laboratory for UV Light-Emitting Materials and Technology of Ministry of Education, Northeast Normal University, Changchun 130024, China*

[3]*Departamento de Física, Universidad del País Vasco-Euskal Herriko Unibertsitatea, UPV/EHU, 48080 Bilbao, Spain*

[4]*Donostia International Physics Center (DIPC), 20018 Donostia, Spain*

[5]*Centro de Física de Materiales CFM, Centro Mixto CSIC-UPV/EHU, 20018 Donostia, Spain*

(Received 2 August 2021; accepted 22 September 2021; published 5 October 2021)

Electrides, which accommodate excess of electrons in lattice interstitials as anions, usually exhibit interesting properties and broad applications. Until now, most electrides, especially at high pressures, show semiconducting/insulating character arising from the strong localization of interstitial and orbital electrons. However, modulating their connectivity could turn them into metals and even superconductors. In this work, with the aid of first-principles particle swarm optimization, we have identified a series of pressure-induced Li-rich electrides in the Li-Te system, in which hollow Li_n polyhedra accommodate the excess of electrons. With increasing Li content, these electrides undergo an interesting structural evolution. Meanwhile, the connection type of Li_n polyhedra experiences transitions from vertex- or edge sharing, to face sharing, leading to a diverse distribution and connectivity of interstitial electrons. All identified electrides exhibit anionic electrons-dominated metallicity. More interestingly, Li_9Te, with the highest content of Li_6 octahedra, is superconducting with a critical temperature (T_c) of 10.2 K at 75 GPa, which is much higher than typical electrides (e.g., $12CaO \cdot 7Al_2O_3$, Ca_2N, and Y_2C). Its superconductivity mainly originates from the coupling between hybridized electrons (anionic and atomic non-*s*-state ones) and Te-dominated phonons.

DOI: 10.1103/PhysRevB.104.134505

I. INTRODUCTION

Electrides are a relatively uncommon class of matter with electrons confined in lattice interstitials that behave as anions, which have recently attracted great attention [1,2]. Based on the topology of localized electrons, electrides can be identified as zero-dimensional (0D) cavities [3], 1D channels [4–6], 2D planes [7,8], and 3D bulk ones [2,9]. However, the concentration, distribution, and connectivity of interstitial electrons in the electrides have a great influence on their electronic properties. For example, as a representative of 0D electrides, $12CaO \cdot 7Al_2O_3$ ($C12A7 : e^-$) contains anionic electrons in the interconnected crystallographic cages [3]. With increasing the concentration of anionic electrons, more electrons occupy the free space inside the crystal lattice, inducing a transition from insulator to semiconductor, then to metal, and even superconductor [10,11]. A typical 2D electride can be exemplified by Ca_2N, where the anionic electrons are loosely confined in the interlayer space at ambient pressure [7]. Under compression, electronic dimensionality is gradually reduced from 2D to 1D, and then to a 0D electride, resulting in a decrease in the electronic conductivity (e.g., under pressure it shows a transition from metal to semimetal, and then to semiconductor) [12]. On the other hand, electrides generally display fascinating properties dominated by interstitial electrons, such as a low work function [13,14], high catalytic activity [15,16], superconductivity [10,17], and magnetism [18,19], leading to a variety of applications including catalysts, superconductors, magnetic materials, electrode materials, and in electronic devices [15,20–22].

On the other hand, raising pressure has become an effective method to discover new electrides, especially for allotropes of alkali and alkaline-earth metals [23–26] and their compounds [2,27,28]. This is so because with increasing pressure, the enhancement of the orbital energy at interstitials is smaller than that of the atomic orbital, causing electrons to enter interstitial sites, which lowers their structural energy. Especially for *s*-block elements, for instance, Li [23], Na [24], K [29], Mg [26], and Al [30] form rich allotropes with an electride character, which are even insulating [25]. On the other hand, alkali metals have been found to be able to form diverse electrides with *p*-block elements, such as O [31], S [27], C [32], N [2], P [17], Cl [33], I [34], and even with inert gas elements at high pressures [35]. Notably, the pressure-induced Li_6P electride shows a superconducting transition temperature (T_c) up to 39.3 K at 270 GPa. Such a high T_c arises mainly from the dumbbell-like connected interstitial electron states that induce a strong Fermi surface nesting and electron-phonon coupling (EPC) [17]. Recently, another interesting electride Li_5C was predicted to have high T_c of 48.3 K at 210 GPa, in which 2D hexagonal anionic electron topology creates interconnected electronic channels in the lattice interstitials [32].

*a.bergara@ehu.eus

†yanggc468@nenu.edu.cn

Tellurium (Te), as the last nonmetallic element in the chalcogens, is isoelectronic to O and S, and shows a low electronegativity, similar to P and I [36]. More importantly, Te has been predicted to be able to form hydrogen-rich compounds, such as H_4Te with a high T_c of 104 K at 170 GPa [37]. Considering the similarity of Li with H, the ability of Li forming electrides, and the effect of pressure on stabilizing new materials, it is expected that Li and Te are able to form novel Li-rich electrides under pressure.

Herein, potential compounds with $Li_xTe(x = 2–12)$ stoichiometry have been extensively searched from 0 to 100 GPa with the aid of an advanced swarm structural search method. Besides the already known Li_2Te, eight new Li-rich tellurides, *Pm* - 3*m* Li_3Te, *I*4/*mmm* Li_3Te, *Imma* Li_4Te, *Cmmm* Li_5Te, $P2_1/m$ Li_7Te, *C*2/*m* Li_9Te, *C*2/*m* $Li_{10}Te$, and *Cmcm* $Li_{12}Te$, have been predicted to be thermally and dynamically stable. All these Li-rich tellurides are metallic electrides, and present a diverse arrangement of interstitial electrons. More importantly, as Li content increases, superconductivity arises, and T_c gradually increases and peaks at 10.2 K in Li_9Te at 75 GPa. They also exhibit a low work function, comparable to C12A7 : e^- electride.

II. COMPUTATIONAL DETAILS

In order to identify thermodynamically stable structures of Li-Te compounds under pressure, structural prediction was implemented with the swarm-intelligence based CALYPSO program (Crystal structure AnaLYsis by Particle Swarm Optimization) [38,39], which can find the most stable structures just knowing the chemical composition [40–43]. We considered various stoichiometries of $Li_xTe(x = 2–12)$ at the selected pressures of 0, 25, 50, and 100 GPa. The details about the structural search method can be found in the Supplemental Material [44].

Structural optimizations and calculations of the electronic properties were carried out within the density-functional theory [45,46] as implemented in the Vienna *Ab initio* Simulation Pckage (VASP) [47]. Considering both accuracy and computational efficiency, the Perdew-Burke-Ernzerhof generalized gradient approximation (GGA) [48,49] exchange and correlation functional was used. The scalar relativistic projector augmented wave (PAW) [50] pseudopotentials were adopted to describe electron-ion interactions, with $1s^2 2s^1$ and $5s^2 5p^4$ valence electrons for Li and Te atoms, respectively. The reliability of adopted pseudopotentials for Li and Te is confirmed by the perfect fit of Birch-Murnaghan equation of states derived from PAW and full-potential linearized augmented plane-wave methods as implemented in WIEN2K (Fig. S0) [51]. The cutoff energy was set at 800 eV, and Monkhorst-Pack [52] *k*-point grids with a reciprocal space resolution of $2\pi \times 0.03$ Å^{-1} in the Brillouin zone were selected to ensure that all enthalpy calculations converged to less than 1 meV per atom. The thermodynamical stability of each lithium telluride stoichiometry with respect to elemental Li and Te solids at each pressure can be evaluated by calculating the formation enthalpy as [53]

$$\Delta H(Li_xTe) = [H(Li_xTe) - xH(Li) - H(Te)]/(x + 1). \quad (1)$$

Here, $H(Li_xTe)$, $H(Li)$, and $H(Te)$ are the enthalpies of the studied stoichiometry, elemental Li, and Te solids under the corresponding pressure, respectively.

The dynamical stability can be determined by calculating phonon frequencies using the supercell finite displacement method [54] with the PHONOPY code [55]. Electron-phonon coupling (EPC) calculations are carried out with the density functional perturbation (linear response) theory as implemented in the QUANTUM ESPRESSO package [56]. The pseudopotential, *k* points, and energy cutoff for wave functions are tested to achieve a pressure consistent with the optimized results obtained with the VASP package, and a good total energy convergence of 0.01 eV/atom. The T_c of all the metallic Li-Te phases is estimated with the McMillan-Allen-Dynes formula [57–59]. Details can be found in the Supplemental Material [44]. The work function (Φ) of a metal is calculated considering a surface slab with a thickness of at least ten atoms. The vacuum distance is set to 20 Å, and a slab supercell is made with $a, b > 10$ Å. The Φ value is determined considering the difference between the vacuum potential and the Fermi level of the slab [13].

III. RESULTS AND DISCUSSION

A. Phase stability

Extensive structural searches are performed on various $Li_xTe(x = 2–12)$ compositions at 0 K and selected pressures of 0, 25, 50, and 100 GPa. The structure with the lowest enthalpy was used to evaluate the stability of different Li-Te compositions according to Eq. (1). The relative thermodynamic stability of the Li-Te compounds with various Li contents at different pressures is shown in the convex hull in Fig. 1(a). Thermally stable phases, represented with filled circles, lie on the global stability line, whereas compositions with hollow circles are metastable in terms of decomposition into other Li_xTe compounds or elemental Li and Te solids. The emerging stable phases with increasing pressure are highlighted in Fig. 1(a). Furthermore, all thermally stable phases are also dynamically stable, as the calculated phonon spectra do not present any imaginary frequency modes (Fig. S1).

In order to determine the stable pressure range of predicted Li-Te compounds, their enthalpy differences are calculated with respect to adjacent stable compositions with a pressure interval of 5 GPa. The pressure-composition phase diagram is shown in Fig. 1(b). In addition to the already known stable antifluorite Li_2Te (*Fm*-3*m* phase) at 0 GPa [64,65], a continuous phase transition is found from *Fm*-3*m* to *Pnma* at 4.8 GPa, then to the $P6_3/mmc$ phase at 19.4 GPa, and finally to the *P*4/*nmm* structure at 96.5 GPa. The atomic arrangement and electronic bands are shown in Figs. S2 and S3, respectively. All three high-pressure phases of Li_2Te are semiconductors with indirect gaps. For Li-rich compositions, two Li_3Te phases emerge with increasing pressure: *Pm*-3*m* Li_3Te is stable between 4 and 85.6 GPa, while *I*4/*mmm* Li_3Te stabilizes above 85.9 GPa. *Imma* Li_4Te and *Cmcm* Li_5Te start to be stable above 34 and 40 GPa, respectively. For Li-richer compositions, $P2_1/m$ Li_7Te and *C*2/*m* Li_9Te become stable in the pressure ranges of 28.5–85.6 GPa, and 16.7–64.1 GPa,

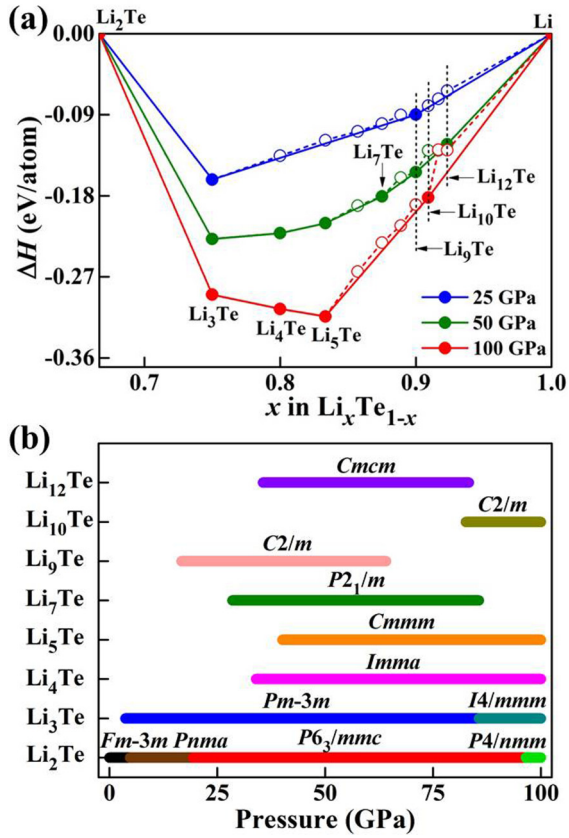

FIG. 1. (a) Phase stabilities of various Li-Te compounds at 0, 25, 50, and 100 GPa. The Fm-3m, I-43d, and $Cmca$-24 structures of elemental solid Li were used to calculate the formation enthalpies [60–62]. Elemental solid Te with phases I ($P3_121$), V (Im-3m), VI ($I4/mmm$), and VII (Fm-3m) were used [63]. (b) Schematic illustration of the pressure stability region of Li-Te compounds.

respectively. For $C2/m$ $Li_{10}Te$ and $Cmcm$ $Li_{12}Te$, their stable pressures are above 82.6 and 35.6 GPa, respectively.

Analyzing the interactions between atoms, the electron localization function (ELF) [66] in Fig. S4 indicates that all the stable Li-Te compounds show an electronic depletion near Li atoms and accumulation around Te atoms, revealing a charge transfer from Li to Te, associated with Li–Te ionic bonds. This can be attributed to the large electronegativity difference between Li (0.98) and Te (2.1) [67]. The transferred charge is shown in Table S1, and will be discussed later. Table S2 shows the distance between nearest-neighbor Li atoms (<2.5 Å) for Li-rich Li_xTe ($x = 3$, 4, 5, 7, 9, 10, and 12), which are much smaller than in the most stable body-centered cubic (bcc) Li (3.01 Å) at ambient pressure [68,69], demonstrating a metallic interaction between Li atoms. However, the distances between the nearest-neighbor Te atoms are much higher than that in elemental $P3_121$ Te (2.89 Å) at ambient pressure. Therefore, ionic Li–Te bonds and metallic Li-Li interaction are responsible for the structural stability of Li-Te compounds.

B. Crystal structure

Figure 2 presents the structures of Li-rich Li_xTe ($x = 3$, 4, 5, 7, 9, 10, and 12) compounds, which exhibit a fairly similar structural characterization, despite having different composition and symmetry. In detail, both Pm-3m and $I4/mmm$ Li_3Te are composed of $TeLi_{12}$ cuboctahedra but with distinct arrangements, causing different symmetries. Li_4Te stabilizes into an orthorhombic structure [space group $Imma$, Fig. 2(c)], in which the coordination of Te increases to 13-fold. As x in Li_xTe increases to 5, 7, and 9, their structures have $Cmmm$, $P2_1/m$, and $C2/m$ symmetries [Fig. 2(d)–2(f)], respectively. In these three structures each Te atom has a 14-fold coordination, despite having different $TeLi_{14}$ configurations. It is worth noting that although Li_xTe ($x = 3$, 4, 5, 7, and 9) have different symmetries and basic structural units, all of them contain hollow Li_6 octahedra, which are surrounded by $TeLi_m$ polyhedra with different connection types (Table S3). With a further increase of the Li ratio, e.g., in $C2/m$ $Li_{10}Te$, the coordination numbers in $TeLi_m$ and Li_n polyhedra increase to 16 and 8 [Fig. 2(g)], respectively. However, in $Cmcm$ $Li_{12}Te$ [Fig. 2(h)], the coordination of Te decreases to 14-fold. Meanwhile, the coexistence of Li_6, Li_7, and Li_8 polyhedra strengthens the interaction between Li atoms and stabilizes the structure.

On the whole, all Li-rich tellurides are composed of interconnected $TeLi_m$ and Li_n polyhedra. The type of connection between $TeLi_m$ and Li_n polyhedra is summarized in Table S3, and discussed in detail below. Among them, Li_9Te has the highest content of Li_6 octahedra (Table S1), and $Li_{10}Te$ has the largest Li_n polyhedra (face-sharing Li_8 enneahedra). Compared to other Li-rich Li-S [27] and Li-I [34] compounds, the same two phases (Li_3Te and Li_5Te) are found in the Li-Te system, because Te has the same valence electrons as S and similar electronegativity to I. The $TeLi_{14}$ unit in Li_7Te and Li_9Te is similar to those in $P6/mmm$ Li_5P [70] and R-3m H_4Te [37].

C. Electride character

The abundant Li_n polyhedra provide a great possibility to accommodate additional electrons, forming electrides like other Li-rich compounds (e.g., Li_4N [2], Li_5P [70], Li_6P [17], Li_3S [27], Li_6O [31], and Li_5I [34]). As expected, all Li-rich Li_xTe show distinct localized interstitial electrons according to the ELF isosurfaces (Fig. S4), confirming their electride character. In order to give an idea of the distribution of these interstitial electrons, we plot the ELF maps of all the electrides in different planes (Fig. 3).

In either Pm-3m or $I4/mmm$ Li_3Te, interstitial electrons are confined in the vertex-sharing Li_6 octahedra and distributed in (110) and (001) planes [Figs. 3(a) and 3(b)], forming 0D electrides. In $Imma$ Li_4Te, the interstitial electrons are also localized in the Li_6 octahedra, but relatively concentrated and clearly interconnected [Fig. 3(c)]. This is due to the lumped distribution of the Li_6 octahedra and the change of connection from vertex- to face sharing (Table S3). $Cmmm$ Li_5Te contains interstitial electrons linked by the surrounding free-electron gas [Fig. 3(d)] [71], which is weaker than in Li_4Te, corresponding to edge-sharing Li_6 octahedra. For clarity, the schematic connectivity of Li_n polyhedra in all Li-rich electrides is shown in Fig. S5. Therefore, the connection type between the polyhedra that host anionic electrons determines the connectivity of localized electrons and the

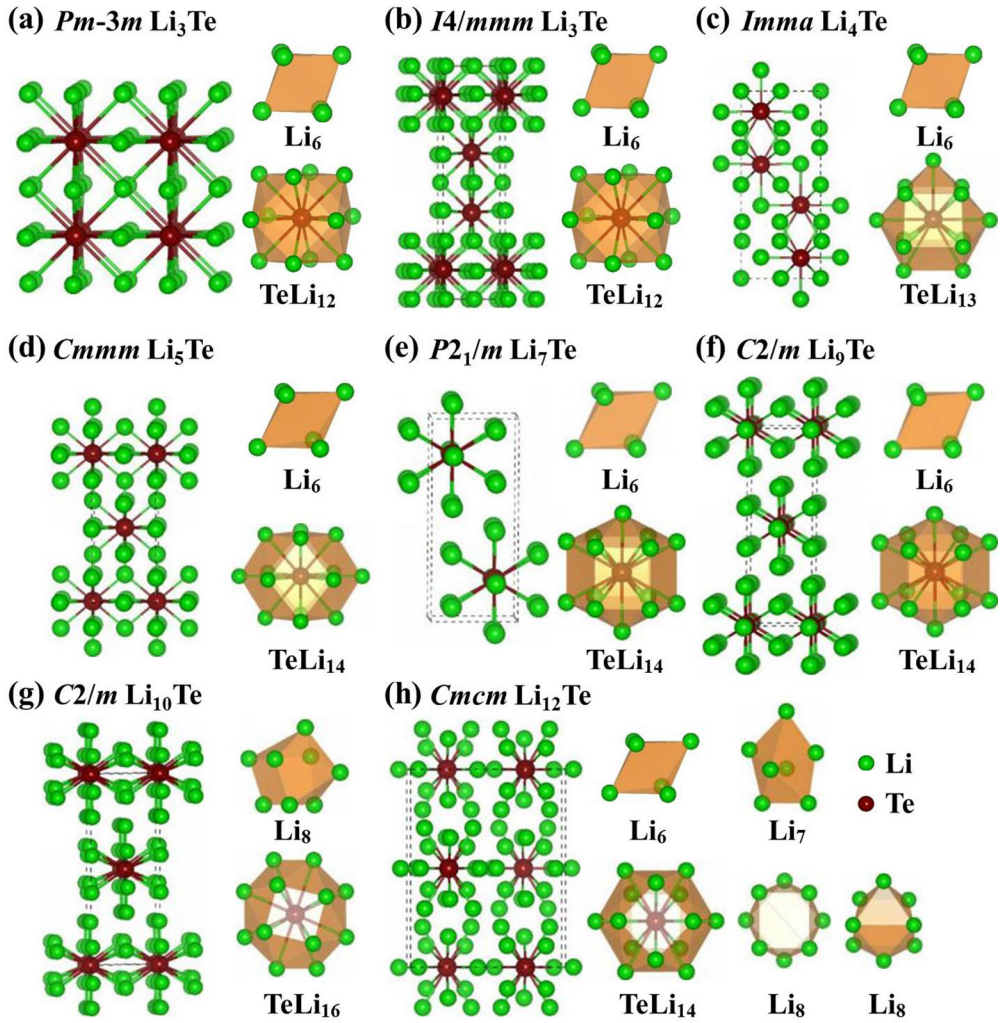

FIG. 2. Structural features of stable Li-rich tellurides at high pressures. (a) *Pm*-3*m* Li_3Te at 50 GPa, (b) *I*4/*mmm* Li_3Te at 100 GPa, (c) *Imma* Li_4Te at 50 GPa, (d) *Cmmm* Li_5Te at 50 GPa, (e) $P2_1/m$ Li_7Te at 50 GPa, (f) $C2/m$ Li_9Te at 50 GPa, (g) $C2/m$ $Li_{10}Te$ at 100 GPa, and (h) *Cmcm* $Li_{12}Te$ at 50 GPa. In all these structures, green and purple spheres represent Li and Te atoms, respectively.

dimensionality of the electrides. A similar phenomenon is observed in metallic $P6_3/m$ Sr_3CrN_3 and Ba_3CrN_3 [6]. There are 1D channels made up of face-sharing $(SrN)_6$ or $(BaN)_6$ polyhedra arranged along the *c* axis that accommodate anionic electrons (Fig. S6). *R*-3m Y_2C [72,73] and Ca_2N [7,74] contain 2D interstitial regions consisting of edge-sharing Y_6 and Ca_6 octahedra in the *ab* plane, respectively, where anionic electrons are confined. Such high connectivity of anionic electron is in favor of the electronic conductivity.

Interestingly, the anionic electrons in $P2_1/m$ Li_7Te and $C2/m$ Li_9Te show a similar distribution: both sunflower- and arc-shaped for them [Figs. 3(e) and 3(f)]. Their anionic electrons are still confined in the Li_6 octahedra, but the connection type between the Li_6 octahedra changes to coexistence of face- and edge sharing (Table S3). With further increasing the Li content, the configuration of Li_n polyhedra becomes complex. As shown in Table S3 and Fig. S5, the coordination of the Li_n polyhedra increases to eightfold in $C2/m$ $Li_{10}Te$, and six-, seven-, and eightfold in *Cmcm* $Li_{12}Te$. The interstitial electrons exhibit a zigzaglike distribution in $C2/m$ $Li_{10}Te$ [Fig. 3(g)], and U- and necklacelike ones in *Cmcm* $Li_{12}Te$ [Fig. 3(h)].

In general, Li and Te have a formal oxidation state of +1 and −2, respectively. Thus, these Li-Te electrides should have the following theoretical anionic electrons: one e^- for Li_3Te, two e^- for Li_4Te, and three e^- for Li_5Te per formula unit (f.u.), and so on. Based on this, we found that the amount of theoretical anionic electrons is closely associated with that of Li_6 octahedra: they turn out to be the same except for Li_5Te (Table S1). In other words, about one electron could be transferred for each Li_6 octahedron. Consequently, Li_9Te has the highest content of anionic electrons fully confined in Li_6 octahedra. In addition, based on the amount of Li_8 enneahedra in the $Li_{10}Te$ lattice unit (8 in 2 f.u.), each Li_8 enneahedron might accommodate about two electrons.

In order to verify the above assumptions, Bader charge analysis is used to study the charge transfer from Li to Te and lattice interstitials (Table S1). Following our expectations, the anionic electrons increase with the Li content, as observed in Li_3Te : $0.25e^-$, Li_4Te : $0.94e^-$, Li_5Te : $1.28e^-$, Li_7Te : $2.62e^-$, and Li_9Te : $3.67e^-$ at 50 GPa, showing the highest concentration of anionic electrons in Li_9Te. In addition, the average anionic electrons in the Li_8 enneahedra of $Li_{10}Te$ is almost double that in the Li_6 octahedra in other Li-Te

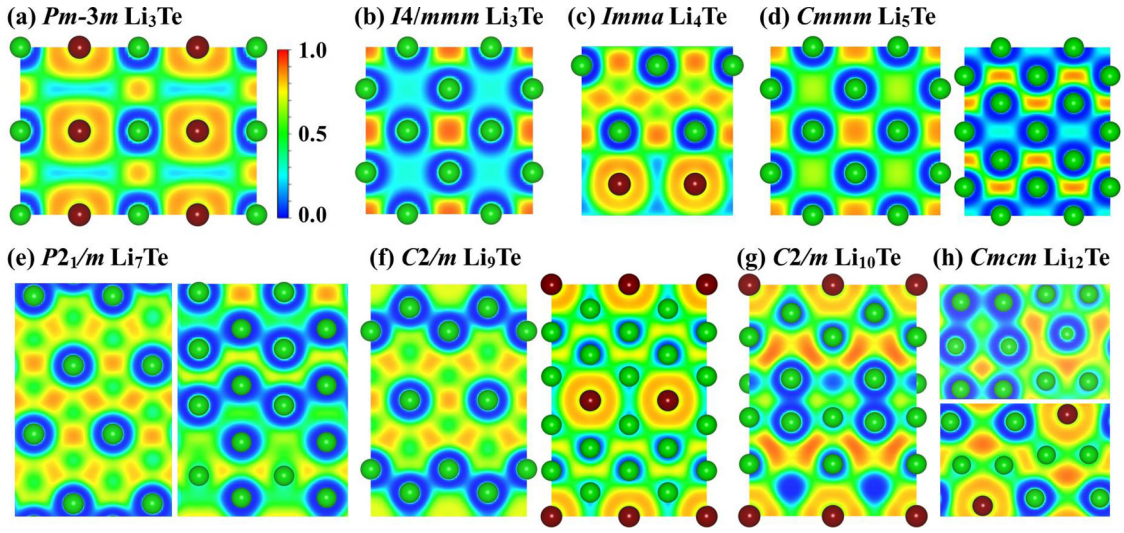

FIG. 3. ELF maps of Li-rich tellurides at high pressure. (a) *Pm*-3*m* Li_3Te at 50 GPa in the (110) plane, (b) *I*4/*mmm* Li_3Te at 100 GPa in the (001) plane, (c) *Imma* Li_4Te at 50 GPa in the (010) plane, (d) *Cmmm* Li_5Te at 50 GPa in the (010) (left) and (001) (right) planes, (e) $P2_1/m$ Li_7Te at 50 GPa in (*hkl* = 13.978, 1, 58.75) (left) and (*hkl* = 1.276, 0, 1) (right) planes, (f) *C*2/*m* Li_9Te at 50 GPa in (*hkl* = −1, 0, 2.089) (left) and (001) planes, (g) *C*2/*m* $Li_{10}Te$ at 100 GPa in the (101) plane, and (h) *Cmcm* $Li_{12}Te$ at 50 GPa in (*hkl* = 1.853, 1, 0) (above) and (100) (below) planes.

electrides (Table S1). The presence of slightly less anionic electrons in $Li_{10}Te$ ($Li_{10}Te$: 3.54e^- at 100 GPa) than in Li_9Te is mainly attributed to its higher pressure. The average charge lost by each Li atom is in the range of 0.67–0.77 e^-. Each Te atom can gain more than two electrons donated by Li atoms, especially in compounds with high Li content, indicating negative oxidation states of Te beyond −2. These extra electrons can occupy Te 5*d* orbitals, as demonstrated by the projected density of states (PDOS). A similar phenomenon has been reported by Miao's group [34] in the Li_5I electride. Overall, the charge localized in Li_n polyhedra is lower than the theoretical anionic electrons, which is mainly attributed to Bader charge analysis underestimating the amount of charge transfer, as observed in typical ionic compounds, e.g., CsF [41].

In short, the anionic electrons in these Li-Te electrides are closely related to the Li content. For Li_xTe (x = 3, 4, 5, 7, and 9), the anionic electrons are localized in the Li_6 octahedra, and their connectivity is gradually enhanced with the Li content, due to the transition of Li_6 octahedra from vertex-, edge-, to face sharing. For $Li_{10}Te$ and $Li_{12}Te$, the Li_n polyhedra accommodating anionic electrons change significantly, leading to a more diverse and complex distribution of anionic electrons.

D. Electronic property and superconductivity

Considering that electrides can exhibit elusory electronic conductivity, such as a semiconducting character in high-pressure Li (*C*2 and *Aba*2) [75], Ca_2N-II, Sr_2N-II, and Ba_2N-IV phases [76], as well as superconductivity, as in Li_5C [32] and Ca_3S [77], we subsequently explored the electronic properties of pressure-induced Li-Te electrides. Unexpectedly, all the Li-Te electrides are metallic (Fig. S7) from the electronic band structures based on the GGA-PBE functional. As representative cases, the electronic band structures of *Pm*-3*m* Li_3Te, *C*2/*m* Li_9Te, and *C*2/*m* $Li_{10}Te$ are also calculated with the revised Heyd-Scuseria-Ernzerhof screened hybrid functional (HSE06), verifying that they are metallic (Fig. S8). The PDOS obviously indicates that the interstitial electrons make the main contribution at the Fermi level (Fig. S9), which can be attributed to the good connectivity between anionic electrons [17]. Moreover, there appears strong overlap between anionic and atomic non-*s*-state (Li 2*p*, Te 5*p*, and Te 5*d*) electrons. To further confirm this, we have built a hypothetical system by removing seven electrons from Li_9Te, $[Li_9Te]^{7+}$. The anionic electrons in ELF are completely absent, which is accompanied by the absence of Fermi surfaces corresponding to the bands crossing the Fermi level of Li_9Te [Fig. S10].

Interestingly, Li_9Te, with the highest content of Li_6 octahedra accommodating anionic electrons, not only exhibits a strong hybridization between anionic electrons and atomic orbital electrons (Li 2*p*, Te 5*p*, and Te 5*d*), but also has two remarkable van Hove singularities (vHs) dominated by anionic electrons near the Fermi level [Fig. 4(a)]. These features made us explore its superconductivity based on the Bardeen-Cooper-Schrieffer theory [78] and the McMillan-Allen-Dynes equation [79], yielding a T_c of 4.01 K with an EPC parameter (λ) of 0.50 at 50 GPa using a Coulomb pseudopotential of $\mu^* = 0.1$ (Table I). Eliashberg spectral function and phonon density of states (PHDOS) show that Te-dominated low-frequency phonons (0–6.16 THz) contribute ∼38%, and Li vibrations make the main contribution of ∼62% in a wide frequency range (6.16-28 THz) [Figs. 4(b) and 4(c)]. The combination of the PDOS composition at the Fermi level and the contribution of λ indicates that the superconductivity of Li_9Te is dominated by the coupling between hybridized anionic/atomic non-*s*-state (Li 2*p*, Te 5*p*, and Te 5*d*) electrons and Li-dominated phonons [80].

Subsequently, we explore the pressure-dependent superconductivity of Li_9Te at 25, 50, 65, and 75 GPa. As shown in Fig. 4(d), T_c increases with pressure and reaches 10.2 K at 75 GPa, which is larger than that in typical electrides

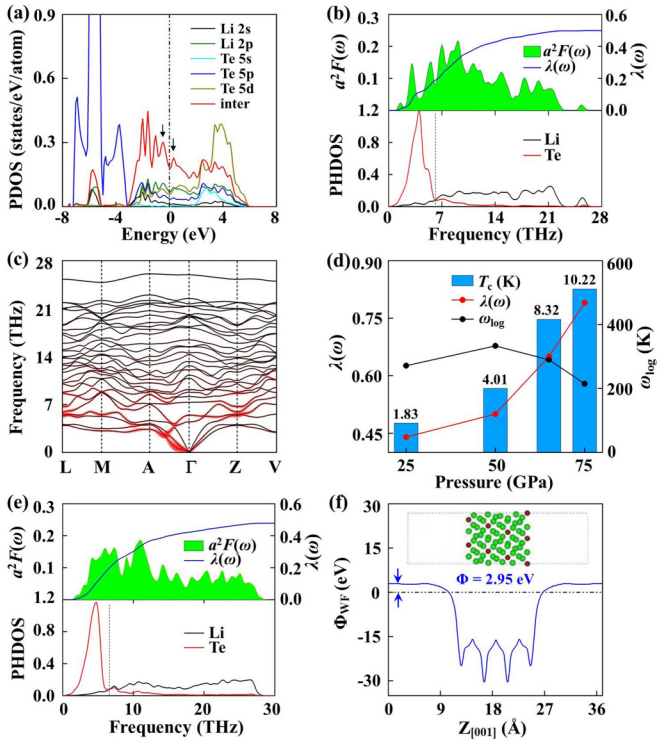

FIG. 4. (a) PDOS of $C2/m$ Li_9Te at 50 GPa. PHDOS, Eliashberg spectral function, and frequency-dependent electron-phonon coupling parameters $\lambda(\omega)$ of (b) $C2/m$ Li_9Te at 50 GPa and (e) $C2/m$ $Li_{10}Te$ at 100 GPa. (c) The calculated phonon dispersion curves of $C2/m$ Li_9Te at 75 GPa. The area of each circle is proportional to the partial electron-phonon coupling, $\lambda_{q,v}$. (d) Pressure-dependent $\lambda(\omega)$, ω_{log}, and T_c of $C2/m$ Li_9Te. (f) The work function of $C2/m$ $Li_{10}Te$ at 100 GPa. The Fermi level is set to zero. The inset displays the corresponding slab with a thickness of at least ten atoms.

(e.g., 0.4 K for C12A7 : e^- [10], 4.7 K for Ca_2N [81], and 0.33–0.59 K for Y_2C [82,83]), and comparable to 9.4 K for Nb_5Ir_3 [84]. On the other hand, the pressure-induced increase of T_c shows the same trend as in other electrides C12A7 : e^- [85], Ca_3Si [86], and Li_5C [32], but is opposite to Li_6P [17]. Analyzing the pressure dependence of λ and the logarithmic average phonon frequency (ω_{log}), it is apparent that pressure-induced increase of T_c in Li_9Te is dominated by the enhancement of λ [Fig. 4(d)]. ω_{log} shows a smooth trend to first increase and then decrease with pressure, meaning it has a little influence on the T_c evolution of Li_9Te. The dominance of λ in T_c is very similar to that of the 1D electride Ca_3Si [86]. It should be noted that Li_9Te is dynamically stable and thermodynamically metastable, with a decomposition enthalpy of only 2.31 meV/atom with respect to Li_7Te and $Li_{12}Te$ at 75 GPa. However, it is within the range (50 meV/atom) for experimental synthesis [87].

We now explore the origin of pressure-induced increase of λ. With increasing pressure, the PDOS of anionic electrons at the Fermi level decreases slightly, with an associated small increase of Li 2*p*, Te 5*p*, and Te 5*d* contributions (Fig. S11). This indicates a potential charge transfer from lattice interstitials to these atomic orbitals and, therefore, a stronger interaction between anionic and non-*s*-state atomic electrons, is expected, which is also confirmed by the Bader charge analysis (Table S4). On the other hand, acoustic branches in the phonon spectra soften with pressure (Fig. S12), which is also associated with the promotion of λ and superconductivity, as it is observed in some superconducting hydrides [88–90]. Correspondingly, the Te's contribution to the total λ gradually increases from 35.6% at 25 GPa, to 38.0% at 50 GPa, to 47.0% at 65 GPa, and to 58.2% at 75 GPa (Table S5). Therefore, pressure-induced enhancement of electron hybridization and phonon softening lead to the increasing of λ with pressure. In addition, through electron- or hole doping, the T_c value is also expected to be enhanced by shifting the Fermi level to adjacent vHs, as shown in H_3S [91]. $Li_{10}Te$, with the largest cavity unit (face-sharing Li_8 enneahedra), is also expected to be a high-T_c superconducting electride. However, unlike Li_9Te, the lack of vHs and the low PDOS contribution at the Fermi level [Fig. S9(g)] as well as feeble phonon softening [Fig. S1(j)] lead to relatively weak EPC with $\lambda = 0.48$ in $Li_{10}Te$ [Fig. 4(e)], corresponding to T_c of ∼4 K at 100 GPa. Te-dominated phonons contribute 40.8% to the total λ in the frequency range of 0–6.7 THz, and Li atom contributes 59.2% between 6.7 and 30 THz, which is in contrast with Li_9Te. Furthermore, other Li-Te electrides exhibit much lower T_c values (<1 K) than Li_9Te and $Li_{10}Te$ (Table I), which can be attributed to that the low concentration and isolated anionic electrons associated with the low content of Li induce a weaker EPC.

E. Low work function

High interstitial electronic concentrations (N_e) and low work functions are two fascinating properties of electrides.

TABLE I. The EPC parameter (λ), ω_{log} (K), T_c, interstitial electron concentration (N_e) of Li-rich tellurides, and the work function (Φ) on different slabs.

Phase	Pressure(GPa)	λ	ω_{log} (K)	T_c (K)	N_e ($\times 10^{22}$ cm^{-3})	Work function (eV)		
						(100)	(010)	(001)
Pm-3*m* Li_3Te	50	0.15	439.69	0.00	0.59	4.13	4.13	4.13
Imma Li_4Te	50	0.25	428.22	0.02	1.89	3.80	3.83	2.83
Cmmm Li_5Te	50	0.24	427.90	0.01	2.24	3.93	3.55	4.34
$P2_1/m$ Li_7Te	50	0.32	450.35	0.43	3.54	3.69	3.79	4.03
$C2/m$ Li_9Te	50	0.50	333.16	4.01	4.04	3.65	3.82	4.05
$C2/m$ $Li_{10}Te$	100	0.48	395.15	4.00	4.66	3.74	4.44	2.95

For instance, C12A7 : e^- shows a high N_e of 2.33×10^{21} cm^{-3}, and a low work function of 2.4 eV [14], leading to important applications such as catalysts and electron field emitters [20]. On the other hand, the low-dimensional localized electrons in the interstitial voids of the electrides easily lead to a low work function [2]. Table I shows the calculated interstitial electron concentration (N_e) based on the Bader charge analysis, and the work function of Li-rich electrides for a slab with a thickness of ten atoms in different directions. Most of Li-rich tellurides show a N_e higher than in C12A7 : e^- and Ca_2N (1.33×10^{22} cm^{-3}). More importantly, their work function values are lower than that of elemental Al (4.28 eV). Specifically, the work function of $C2/m$ $Li_{10}Te$ is as low as 2.95 eV in the (001) direction [Fig. 4(f)], and that of *Imma* Li_4Te even reaches 2.83 eV (Table I). Such a low work function is comparable with the R-3m Y_2C electride (2.9 eV), [8] and the Li metal (2.9 eV), [93] and is much lower than Y_5Si_3 (3.5 eV), [92] which is an excellent catalyst for ammonia synthesis. Therefore, high interstitial electron concentrations and low work functions may endow Li-rich tellurides with potential applications, such as in catalysis and electric devices.

IV. CONCLUSION

In summary, we have searched pressure-induced Li-rich tellurides (Li_xTe, $x = 2$–12) under pressure up to 100 GPa by first-principles calculations. In addition to reproducing the already known Li_2Te compound, we have found eight stable Li-rich tellurides. Although presenting different symmetries, they all consist of interconnected $TeLi_m$ and Li_n polyhedra. The hollow Li_n polyhedra can accommodate extra electrons, leading to the formation of electrides. The distribution of interstitial electrons depends on the coordination and connection type of the Li_n polyhedra, and becomes more diverse and complex with increasing the Li content. Interestingly, all Li-rich electrides are metallic, even for Pm-3m and $I4/mmm$ Li_3Te with weakly interconnected anionic electrons. Most of them are superconducting. Li_9Te and $Li_{10}Te$ have a much higher T_c than the others, due to a high content of Li_6 octahedra in the former and a large cavity unit (Li_8 enneahedra) in the latter. In addition, Li-rich tellurides exhibit a high interstitial electron concentration, and a low work function. Our work presents members of pressure-induced electrides with superconductivity and a low work function.

ACKNOWLEDGMENTS

The authors acknowledge the funding support from the Natural Science Foundation of China under Grants No. 21873017 and No. 21573037, the Postdoctoral Science Foundation of China under Grant No. 2013M541283, the Natural Science Foundation of Jilin Province (Grant No. 20190201231JC), and the Natural Science Foundation of Hebei Province (Grant No. B2021203030). The work was carried out at National Supercomputer Center in Tianjin, and the calculations were performed on TianHe-1 (A). A.B. acknowledges financial support from the Spanish Ministry of Science and Innovation (Grant No. PID2019-105488GB-I00).

The authors declare no competing financial interest.

[1] J. L. Dye, Science **301**, 607 (2003).
[2] Y. Tsuji, P. L. V. K. Dasari, S. F. Elatresh, R. Hoffmann, and N. W. Ashcroft, J. Am. Chem. Soc. **138**, 14108 (2016).
[3] S. Matsuishi, Y. Toda, M. Miyakawa, K. Hayashi, T. Kamiya, M. Hirano, I. Tanaka, and H. Hosono, Science **301**, 626 (2003).
[4] Y. Zhang, Z. Xiao, T. Kamiya, and H. Hosono, J. Phys. Chem. Lett. **6**, 4966 (2015).
[5] L. A. Burton, F. Ricci, W. Chen, G.-M. Rignanese, and G. Hautier, Chem. Mater. **30**, 7521 (2018).
[6] P. Chanhom, K. E. Fritz, L. A. Burton, J. Kloppenburg, Y. Filinchuk, A. Senyshyn, M. Wang, Z. Feng, N. Insin, J. Suntivich *et al.*, J. Am. Chem. Soc. **141**, 10595 (2019).
[7] K. Lee, S. W. Kim, Y. Toda, S. Matsuishi, and H. Hosono, Nature (London) **494**, 336 (2013).
[8] X. Zhang, Z. Xiao, H. Lei, Y. Toda, S. Matsuishi, T. Kamiya, S. Ueda, and H. Hosono, Chem. Mater. **26**, 6638 (2014).
[9] Y. Zhang, H. Wang, Y. Wang, L. Zhang, and Y. Ma, Phys. Rev. X **7**, 011017 (2017).
[10] M. Miyakawa, S. W. Kim, M. Hirano, Y. Kohama, H. Kawaji, T. Atake, H. Ikegami, K. Kono, and H. Hosono, J. Am. Chem. Soc. **129**, 7270 (2007).
[11] S. W. Kim, M. Miyakawa, M. Hirano, Y. Kohama, H. Kawaji, T. Atake, H. Ikegami, K. Kono, and H. Hosono, Mater. Trans. **49**, 1748 (2008).
[12] H. Tang, B. Wan, B. Gao, Y. Muraba, Q. Qin, B. Yan, P. Chen, Q. Hu, D. Zhang, L. Wu *et al.*, Adv. Sci. **5**, 1800666 (2018).
[13] M. A. Uijttewaal, G. A. d. Wijs, and R. A. d. Groot, J. Appl. Phys. **96**, 1751 (2004).
[14] Y. Toda, H. Yanagi, E. Ikenaga, J. J. Kim, M. Kobata, S. Ueda, T. Kamiya, M. Hirano, K. Kobayashi, and H. Hosono, Adv. Mater. **19**, 3564 (2007).
[15] M. Kitano, Y. Inoue, Y. Yamazaki, F. Hayashi, S. Kanbara, S. Matsuishi, T. Yokoyama, S.-W. Kim, M. Hara, and H. Hosono, Nat. Chem. **4**, 934 (2012).
[16] M. Hara, M. Kitano, and H. Hosono, ACS Catal. **7**, 2313 (2017).
[17] Z. Zhao, S. Zhang, T. Yu, H. Xu, A. Bergara, and G. Yang, Phys. Rev. Lett. **122**, 097002 (2019).
[18] J. Park, K. Lee, S. Y. Lee, C. N. Nandadasa, S. Kim, K. H. Lee, Y. H. Lee, H. Hosono, S.-G. Kim, and S. W. Kim, J. Am. Chem. Soc. **139**, 615 (2017).
[19] S. Y. Lee, J.-Y. Hwang, J. Park, C. N. Nandadasa, Y. Kim, J. Bang, K. Lee, K. H. Lee, Y. Zhang, Y. Ma *et al.*, Nat. Commun. **11**, 1526 (2020).
[20] X. Zhang and G. Yang, J. Phys. Chem. Lett. **11**, 3841 (2020).
[21] Y. Toda, S. Matsuishi, K. Hayashi, K. Ueda, T. Kamiya, M. Hirano, and H. Hosono, Adv. Mater. **16**, 685 (2004).
[22] M. M. Menamparambath, J. H. Park, H. S. Yoo, S. P. Patole, J. B. Yoo, S. W. Kim, and S. Baik, Nanoscale **6**, 8844 (2014).
[23] C. J. Pickard and R. J. Needs, Phys. Rev. Lett. **102**, 146401 (2009).
[24] Y. Ma, M. Eremets, A. R. Oganov, Y. Xie, I. Trojan, S. Medvedev, A. O. Lyakhov, M. Valle, and V. Prakapenka, Nature (London) **458**, 182 (2009).

[25] M. Gatti, I. V. Tokatly, and A. Rubio, Phys. Rev. Lett. **104**, 216404 (2010).

[26] P. Li, G. Gao, Y. Wang, and Y. Ma, J. Phys. Chem. C **114**, 21745 (2010).

[27] C. Kokail, C. Heil, and L. Boeri, Phys. Rev. B **94**, 060502(R) (2016).

[28] W. Ming, M. Yoon, M.-H. Du, K. Lee, and S. W. Kim, J. Am. Chem. Soc. **138**, 15336 (2016).

[29] C. J. Pickard and R. J. Needs, Phys. Rev. Lett. **107**, 087201 (2011).

[30] C. J. Pickard and R. J. Needs, Nat. Mater. **9**, 624 (2010).

[31] X. Dong, Y.-L. Li, A. R. Oganov, K. Li, H. Zheng, and H.-k. Mao, Phys. Rev. B **100**, 144104 (2019).

[32] Z. S. Pereira, G. M. Faccin, and E. Z. da Silva, J. Phys. Chem. C **125**, 8899 (2021).

[33] W. Zhang, A. R. Oganov, A. F. Goncharov, Q. Zhu, S. E. Boulfelfel, A. O. Lyakhov, E. Stavrou, M. Somayazulu, V. B. Prakapenka, and Z. Konôpková, Science **342**, 1502 (2013).

[34] J. Botana, J. Brgoch, C. Hou, and M. Miao, Inorg. Chem. **55**, 9377 (2016).

[35] M.-s. Miao, X.-l. Wang, J. Brgoch, F. Spera, M. G. Jackson, G. Kresse, and H.-q. Lin, J. Am. Chem. Soc. **137**, 14122 (2015).

[36] A. L. Allred, J. Inorg. Nucl. Chem. **17**, 215 (1961).

[37] X. Zhong, H. Wang, J. Zhang, H. Liu, S. Zhang, H.-F. Song, G. Yang, L. Zhang, and Y. Ma, Phys. Rev. Lett. **116**, 057002 (2016).

[38] Y. Wang, J. Lv, L. Zhu, and Y. Ma, Phys. Rev. B **82**, 094116 (2010).

[39] Y. Wang, J. Lv, L. Zhu, and Y. Ma, Comput. Phys. Commun. **183**, 2063 (2012).

[40] L. Zhu, H. Wang, Y. Wang, J. Lv, Y. Ma, Q. Cui, Y. Ma, and G. Zou, Phys. Rev. Lett. **106**, 145501 (2011).

[41] M.-s. Miao, Nat. Chem. **5**, 846 (2013).

[42] G. Yang, Y. Wang, and Y. Ma, J. Phys. Chem. Lett. **5**, 2516 (2014).

[43] L. Zhu, H. Liu, C. J. Pickard, G. Zou, and Y. Ma, Nat. Chem. **6**, 644 (2014).

[44] See Supplemental Material at http://link.aps.org/supplemental/10.1103/PhysRevB.104.134505 for computational details, phonon spectra, ELF isosurfaces, electronic band structures and density of states, Bader charge analysis, phonon spectra and EPC parameter of Li9Te at different pressures, and structural information.

[45] P. Hohenberg and W. Kohn, Phys. Rev. **136**, B864 (1964).

[46] W. Kohn and L. J. Sham, Phys. Rev. **140**, A1133 (1965).

[47] G. Kresse and J. Furthmüller, Phys. Rev. B **54**, 11169 (1996).

[48] J. P. Perdew, K. Burke, and M. Ernzerhof, Phys. Rev. Lett. **77**, 3865 (1996).

[49] J. P. Perdew, J. A. Chevary, S. H. Vosko, K. A. Jackson, M. R. Pederson, D. J. Singh, and C. Fiolhais, Phys. Rev. B **46**, 6671 (1992).

[50] P. E. Blöchl, Phys. Rev. B **50**, 17953 (1994).

[51] P. Blaha, K. Schwarz, P. Sorantin, and S. B. Trickey, Comput. Phys. Commun. **59**, 399 (1990).

[52] H. J. Monkhorst and J. D. Pack, Phys. Rev. B **13**, 5188 (1976).

[53] K. Reuter and M. Scheffler, Phys. Rev. B **65**, 035406 (2001).

[54] K. Parlinski, Z. Q. Li, and Y. Kawazoe, Phys. Rev. Lett. **78**, 4063 (1997).

[55] A. Togo, F. Oba, and I. Tanaka, Phys. Rev. B **78**, 134106 (2008).

[56] P. Giannozzi, S. Baroni, N. Bonini, M. Calandra, R. Car, C. Cavazzoni, D. Ceresoli, G. L. Chiarotti, M. Cococcioni, I. Dabo *et al.*, J. Phys.: Condens. Matter **21**, 395502 (2009).

[57] L. N. Oliveira, E. K. U. Gross, and W. Kohn, Phys. Rev. Lett. **60**, 2430 (1988).

[58] M. Lüders, M. A. L. Marques, N. N. Lathiotakis, A. Floris, G. Profeta, L. Fast, A. Continenza, S. Massidda, and E. K. U. Gross, Phys. Rev. B **72**, 024545 (2005).

[59] M. A. L. Marques, M. Lüders, N. N. Lathiotakis, G. Profeta, A. Floris, L. Fast, A. Continenza, E. K. U. Gross, and S. Massidda, Phys. Rev. B **72**, 024546 (2005).

[60] M. Hanfland, K. Syassen, N. E. Christensen, and D. L. Novikov, Nature (London) **408**, 174 (2000).

[61] J. Lv, Y. Wang, L. Zhu, and Y. Ma, Phys. Rev. Lett. **106**, 015503 (2011).

[62] L. Shi and D. A. Papaconstantopoulos, Phys. Rev. B **73**, 184516 (2006).

[63] T. Sugimoto, Y. Akahama, T. Ichikawa, H. Fujihisa, N. Hirao, and Y. Ohishi, J. Phys.: Conf. Ser. **500**, 192018 (2014).

[64] B. Bahloul, L. Amirouche, A. Dekhira, and A. Bentabet, Comput. Mater. Sci. **86**, 49 (2014).

[65] X. D. Zhang and H. F. Shi, Mater. Sci. Technol. **30**, 732 (2014).

[66] S. G. Dale and E. R. Johnson, J. Phys. Chem. A **122**, 9371 (2018).

[67] L. R. Murphy, T. L. Meek, A. L. Allred, and L. C. Allen, J. Phys. Chem. A **104**, 5867 (2000).

[68] R. Berliner, O. Fajen, H. G. Smith, and R. L. Hitterman, Phys. Rev. B **40**, 12086 (1989).

[69] A. Kulkarni, K. Doll, D. L. V. K. Prasad, J. C. Schön, and M. Jansen, Phys. Rev. B **84**, 172101 (2011).

[70] Z. Zhao, L. Liu, T. Yu, G. Yang, and A. Bergara, J. Phys. Chem. C **121**, 21199 (2017).

[71] A. D. Becke and K. E. Edgecombe, J. Chem. Phys. **92**, 5397 (1990).

[72] M. Hiraishi, K. M. Kojima, I. Yamauchi, H. Okabe, S. Takeshita, A. Koda, R. Kadono, X. Zhang, S. Matsuishi, H. Hosono *et al.*, Phys. Rev. B **98**, 041104(R) (2018).

[73] H. Huang, K.-H. Jin, S. Zhang, and F. Liu, Nano Lett. **18**, 1972 (2018).

[74] C. M. Fang, G. A. de Wijs, R. A. de Groot, H. T. Hintzen, and G. de With, Chem. Mater. **12**, 1847 (2000).

[75] Y. Yao, J. S. Tse, and D. D. Klug, Phys. Rev. Lett. **102**, 115503 (2009).

[76] Y. Zhang, W. Wu, Y. Wang, S. A. Yang, and Y. Ma, J. Am. Chem. Soc. **139**, 13798 (2017).

[77] Y.-X. Liu, C. Wang, S. Han, X. Chen, H.-R. Sun, and X.-B. Liu, Chin. Phys. Lett. **38**, 036201 (2021).

[78] J. Bardeen, L. N. Cooper, and J. R. Schrieffer, Phys. Rev. **108**, 1175 (1957).

[79] P. B. Allen and R. C. Dynes, Phys. Rev. B **12**, 905 (1975).

[80] H. Hosono, S.-W. Kim, S. Matsuishi, S. Tanaka, A. Miyake, T. Kagayama, and K. Shimizu, Philos. Trans. R. Soc. A **373**, 20140450 (2015).

[81] X. Zeng, S. Zhao, Z. Li, and J. Yang, Phys. Rev. B **98**, 155443 (2018).

[82] Y. He, J. Alloys Compd. **654**, 180 (2016).

[83] S. Dilmi, S. Saib, and N. Bouarissa, Curr. Appl. Phys. **18**, 1338 (2018).

[84] Y. Zhang, B. Wang, Z. Xiao, Y. Lu, T. Kamiya, Y. Uwatoko, H. Kageyama, and H. Hosono, npj Quantum Mater. **2**, 45 (2017).

[85] S. Tanaka, T. Kato, A. Miyake, T. Kagayama, K. Shimizu, S. W. Kim, S. Matsuishi, and H. Hosono, J. Korean Phys. Soc. **63**, 477 (2013).

[86] B. Sa, R. Xiong, C. Wen, Y.-L. Li, P. Lin, Q. Lin, M. Anpo, and Z. Sun, J. Phys. Chem. C **124**, 7683 (2020).

[87] Y. Hinuma, T. Hatakeyama, Y. Kumagai, L. A. Burton, H. Sato, Y. Muraba, S. Iimura, H. Hiramatsu, I. Tanaka, H. Hosono *et al.*, Nat. Commun. **7**, 11962 (2016).

[88] Y. Li, J. Hao, H. Liu, J. S. Tse, Y. Wang, and Y. Ma, Sci. Rep. **5**, 9948 (2015).

[89] X. Liang, S. Zhao, C. Shao, A. Bergara, H. Liu, L. Wang, R. Sun, Y. Zhang, Y. Gao, Z. Zhao *et al.*, Phys. Rev. B **100**, 184502 (2019).

[90] H. Xie, Y. Yao, X. Feng, D. Duan, H. Song, Z. Zhang, S. Jiang, S. A. T. Redfern, V. Z. Kresin, C. J. Pickard *et al.*, Phys. Rev. Lett. **125**, 217001 (2020).

[91] Y. Ge, F. Zhang, R. P. Dias, R. J. Hemley, and Y. Yao, Mater. Today Phys. **15**, 100330 (2020).

[92] Y. Lu, J. Li, T. Tada, Y. Toda, S. Ueda, T. Yokoyama, M. Kitano, and H. Hosono, J. Am. Chem. Soc. **138**, 3970 (2016).

[93] H. B. Michaelson, J. Appl. Phys. **48**, 4729 (1977).